Vertical velocity structure of marine boundary layer trade wind cumulus clouds

Virendra P. Ghate,[1] Mark A. Miller,[1] and Lynne DiPretore[1]

[1] Oceanic trade wind cumulus clouds not only impact the Earth's radiation budget but also affect the boundary layer (BL) structure. Data from the deployment of Atmospheric Radiation Measurements (ARM)'s Mobile Facility at the island of Graciosa in the Azores is used to study the vertical velocity structure of these clouds. The surface fluxes as reported by the European Centre for Medium-Range Weather Forecasting (ECMWF) analysis model were used to characterize the dynamic structure of the BL. Cloud radar data from nine cases totaling to 114 hours and containing 557 cumulus cloud elements are analyzed to report hourly values of mean reflectivity, mean vertical velocity, cloud fraction, and cloud mass flux. The hourly averaged in-cloud vertical velocity was constant ($\sim$0.35 m s^{-1}) with height, while the average velocity of updrafts and vertically coherent updrafts increased from cloud base to cloud top. The reflectivity did not exhibit any significant changes between all, updraft and coherent updraft samples. The cloud fraction and mass flux showed similar vertical profiles with both having a peak near cloud base. The mass flux contribution of vertically coherent updrafts spanning through the entire cloud layer to the average updraft mass flux was $\sim$62%. The hourly values were classified based on the surface convective velocity scale (w*) as reported by the ECMWF model. The cloud fraction near cloud base during hours with w* less than 0.2 m s^{-1} was $\sim$6% while that during hours with w* greater than 0.6 m s^{-1} was $\sim$9%. The cloud base mass flux during hours with w* greater than 0.6 m s^{-1} was almost double that during hours with w* less than 0.2 m s^{-1}.

1. Introduction

[2] Boundary layer (BL) fair weather cumulus clouds or oceanic trade wind cumulus clouds not only impact the Earth's radiation budget but also affect the BL structure and surface temperature and humidity [*Berg and Kassianov*, 2008]. The hourly cloud coverage of these clouds has been reported to vary from 24 to 35% over the continents [*Berg and Kassianov*, 2008], 15–25% in the tropics [*Kollias and Albrecht*, 2010] and 40% over the subtropical oceans [*Albrecht et al.*, 1995a, 1995b]. *Warren et al.* [1988] have reported that the cumulus cloud amount is about 20% in the trade wind regions and decreases poleward to a value of 3% in the polar region. Boundary layer cumuli are intimately tied to the turbulence in the BL and contribute significantly to the diurnal cycle of the continental BL [*Brown et al.*, 2002]. *Neggers et al.* [2007] and *Tiedtke et al.* [1988] among others have argued that the subtropical oceanic shallow cumulus convection plays an important role in determining the strength and width of the Intertropical Convergence Zone (ITCZ), and hence a reduction in mixing by shallow cumulus in warmer climate may lead to similar large-scale feedbacks. The oceanic trade wind cumuli are particularly important since a significant gap in the knowledge of the mechanics of the transition between subtropical stratocumulus and tropical cumulus exists.

[3] Shallow cumuli in the BL have been the focus of many previous observational field campaigns like Atlantic Trade Wind Experiment ATEX [*Augstein et al.*, 1973], Atlantic Stratocumulus Transition Experiment, ASTEX [*Albrecht et al.*, 1995a, 1995b], Rain In Cumulus Over Ocean, RICO [*Rauber et al.*, 2007], Cloud Land Surface Interaction Campaign, CLASIC and Cumulus Humilis Aerosol Processing Study, CHAPS [*Berg et al.*, 2009] and modeling studies [e.g., *Brown et al.*, 2002; *Zhu and Albrecht*, 2002; *Siebesma et al.*, 2003; *Siebesma and Cuijpers*, 1995]. Many recent modeling studies have used Large Eddy Simulation (LES) models with explicit Bin Microphysics (BM) schemes (LES-BM models) to quantify the aerosol-cloud-precipitation interactions associated with BL cumuli [e.g., *Jiang et al.*, 2006, 2009; *Koren et al.*, 2009] and produce statistical surveys of their expected behavior under a range

[1]Department of Environmental Sciences, Rutgers University, New Brunswick, New Jersey, USA.
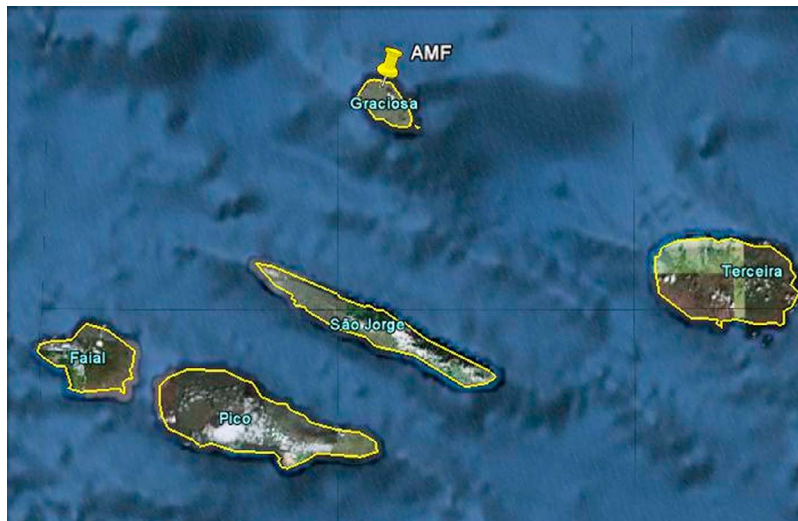
Figure 1. Location of the ARM Mobile Facility (AMF) on the island of Graciosa in the Azores. The AMF is located at 39.08°N, 28.02°W and is 15 m above the sea level. The image was produced using Google Earth application.

of conditions. Since these clouds occur at scales much smaller than a typical grid size of a Global Climate Model (GCM), they are parameterized and several parameterizations have been proposed [e.g., *Albrecht*, 1981; *Berg and Stull*, 2005; *Bretherton et al.*, 2004, *Neggers*, 2009; *Grant*, 2001; *von Salzen and McFarlane*, 2002]. Parameterizations based on mass flux approach require some estimate of vertical velocity in the boundary layer to represent the cloudiness [e.g., *Bretherton et al.*, 2004]. Higher order moments of the vertical velocity are used in parameterizations based on higher order turbulence closure schemes or PDF based schemes [e.g., *Lappen and Randall*, 2001; *Golaz et al.*, 2002]. Despite the importance of fair weather cumulus clouds in the Earth's climate and their vertical velocity structure for proper representation in GCMs, observations of vertical velocity structure of these clouds remain sparse. Most of the previous observations were collected using aircraft in situ instruments that inherently lack vertical coherency [e.g., *Rodts et al.*, 2003]. Recently, observations made by vertically pointing Doppler cloud radar have been used to study the vertical velocity structure of cumulus and stratocumulus clouds [e.g., *Ghate et al.*, 2010; *Kollias and Albrecht*, 2010].

[4] In this study we use observations made at the Atmospheric Radiation Measurements (ARM) Mobile Facility (AMF) deployed at the island of Graciosa in the Azores for the Cloud Aerosol and Precipitation in the Marine Boundary Layer (CAP-MBL) field campaign to quantify the dynamical structure of trade cumulus clouds. The AMF is located at 39.08°N, 28.02°W and is 15 m above the mean seal level (Figure 1). Nine episodes of oceanic trade wind cumulus clouds lasting for 114 h and consisting of 557 individual cloud elements are analyzed. The instrumentation and methodology are described in section 2 followed by a description in section 3 of conditions in which these clouds were observed and their dynamical structure. The variations of the vertical velocity structure of these clouds for different con-

ditions are explored in section 4. Section 5 provides a summary and discussion.

2. Instrumentation, Data, and Methodology

[5] The AMF is located at the northern edge of the island of Graciosa and the winds were predominantly from the northeast quadrant for the study periods (Figure 1). The AMF is equipped with various instruments including a vertically pointing Doppler cloud radar, laser ceilometer, surface condensation particle counter (CPC) and balloon borne soundings. The vertically pointing radar operates at 95 GHz frequency, has polarization ability and is called the *W* band ARM Cloud Radar (WACR). The radar has range resolution of 42 m and temporal resolution of 4 s sufficient to characterize the in-cloud BL turbulence [*Ghate et al.*, 2010]. The radar records the full Doppler spectrum from which the first three Doppler spectral moments, reflectivity, mean Doppler velocity and Doppler spectrum width are calculated. These correspond to the sixth moment of the cloud drop size distribution, the reflectivity weighted vertical air motion of the cloud drops and the standard deviation of reflectivity weighted vertical air motion of the cloud drops respectively. The radar has a sensitivity of −48 dBZ at 1 km, while the reflectivity and mean Doppler velocity have uncertainties of 1 dBZ and 0.1 m s^{-1} respectively. The laser ceilometer operates at 905 nm and reports the first three cloud base heights with 15 s and 15 m resolution, respectively. The CPC is a part of the Aerosol Observing System (AOS) and operates at 780 nm reporting the total concentration of particles ranging from 0.01 μm to 3 μm. Balloon borne radiosondes are launched at the site every 6 h and report the temperature, humidity and winds in the atmospheric column. The cloud fraction was calculated using the WACR data on hourly time scales by dividing the number of samples above the noise threshold by the total number of samples at each radar range gate. Hourly cloud cover was also calculated in a similar fashion from the ceilometer

Table 1. General Characteristics of the Nine Cases Analyzed in This Study[a]

Date (yyyymmdd)	UTC Time	Wind Speed (m s^{-1})	w* (m s^{-1})	ω_{700} (mbar d^{-1})	Inversion $\Delta\theta$ (k)	Inversion Δq (g kg^{-1})	Wind Shear (10^{-3} s^{-1})	CPC (number per cm^3)
20090606	0000–1400	2.78	0.46	64.87	5.89	−6.44	2.5	596
20090615	0800–2400	4.37	0.35	30.58	7.16	−5.76	10.1	944
20090626	1200–2400	4.91	0.61	149.39	-	-	3.25	1066
20090712	0000–2100	5.02	0.55	88.53	5.25	−4.24	0.68	849
20090915a	0000–1200	5.08	0.60	74.44	6.83	−5.07	3.5	711
20090915b	1400–2400	4.97	0.56	107.32	4.85	−3.27	17.93	505
20091016	1400–2400	3.76	0.22	81.60	-	-	3.0	782
20091017	0000–0700	3.71	0.05	68.32	-	-	0.42	713
20091019	0000–1200	6.40	0.24	43.06	4.41	−3.09	4.5	614

[a]The columns represent date, time, surface wind speed, surface convective velocity scale (w*), large-scale vertical velocity at 700 mbar (ω_{700}), potential temperature jump across the BL inversion, specific humidity jump across the BL inversion, wind shear in the cloud layer, and surface aerosol number concentration as measured by CPC. For dates, yyyymmdd denotes year, month, and day; read 20090615 as 15 June 2009. All the variables are calculated from the radiosondes launched during the cases, except w* and ω_{700}, which are as reported by the ECMWF model.

recorded first cloud base height data. The cloud fraction determined using WACR data yielded a vertical profile of cloud fraction while that determined using ceilometer data yielded cloud cover for the entire atmospheric column below 7 km. The ceilometer cloud cover was always higher than the WACR reported cloud fraction at all levels primarily due to peculiar cloud structure of BL cumulus clouds as discussed in detail by *Berg and Kassianov* [2008] and *Neggers et al.* [2003].

[6] The average cloud fraction of BL trade cumulus cloud is ~6% near cloud base (discussed later) and less than 1% just below the trade wind inversion, with the average ceilometer cloud cover of ~25%. Hence, only one in four radiosondes launched in a fair weather environment *might* pass through the cloud, with even smaller chances of a radiosonde passing through the entire cloud layer. As stated earlier, radiosondes are launched at the site every six hours. During the nine cases discussed in this study, total of 24 radiosondes were launched, none of which recorded a RH of 100% with only five of them recording RH greater than 95%. This might be due to combination of slow response of the RH sensor and the radiosonde being in a saturated environment for a small time. Further, it occurs that a radiosonde passing through a cloud element will exhibit a larger Convective Available Potential Energy (CAPE) than the radiosonde not passing through cloud element [*Siebesma et al.* 2003, Figure 7c]. Also, some of the radiosondes did not pass through the cloud but passed through the detraining flow from the active cloud, yielding an anomalously high humidity value above the inversion. Hence, it is difficult to get the mean environmental conditions from radiosondes launched at a coarser temporal interval. It has been suggested by *Stevens et al.* [2001] that the observational studies should provide robust cloud statistics as a function of mean environmental conditions and it is difficult to observe the environmental temperature and humidity structure through radiosondes launched at a 6 h resolution. Despite the above mentioned shortcomings, data from the balloon borne radiosondes present the only opportunity to gain insights into the BL temperature and humidity structure. Although the inversion strength, wind shear etc. calculated from an individual radiosonde might not represent the environmental conditions accurately, an average of these parameters calculated from multiple soundings presents some measure of the BL structure. Hence, presented in this study

(Table 1) are averages of inversion strength and wind shear over a particular case calculated using the radiosondes launched during those cases.

[7] The challenges posed by a broken cloud field are also evident in the data from other instruments. The microwave radiometer retrieves the values of liquid water path (LWP) at a 20 s resolution with the field of view having horizontal dimension of 80 m at 1 km height. As most of the shallow cumulus clouds have horizontal dimension of less than 500 m and depth of ~200 m (discussed later), the microwave radiometer observations are too coarse temporally and spatially to accurately observe the LWP associated with these clouds. Further, the clouds sampled over the facility were of marine origin while the surface met suite and flux suit present at the AMF reported the met data and surface turbulent fluxes over the island. The lifting condensation level (LCL) calculated from the AMF met measurements was much higher than the observed cloud base heights further confirming that the sampled clouds were of marine origin rather than due to daytime island heating.

[8] The limitations described above necessitated the use of model data to characterize the surface turbulent fluxes and surface meteorology during the study periods. Data from the European Centre for Medium-Range Weather Forecasting (ECMWF) model are used to characterize the dynamic structure of the boundary layer at the time of the observations. The model data had resolution of 0.56° × 0.56° and the data for the grid point centered at 39.01°N and 28.12°W are used here. Hourly averaged values of surface sensible heat flux (SHF) and surface latent heat flux (LHF) from the model output were used to obtain the surface convective velocity scale (w*) per Stull (1988) using the LCL as scaling height. The AMF is located within 100 m of the island's northern edge. The average w* from the ECMWF model was 0.52 m s^{-1} while the average w* from the flux suite on the island was 1.65 m s^{-1}. The average cloud base height of the cumulus clouds was 570 m (discussed later), while the average lifting condensation level calculated from the surface met station located on the island was 653.43 m. The time scale for eddies within the marine atmospheric mixed layer was 570/0.52 = 18.27 min. The time taken by an eddy generated due to island heating to reach the observed cloud base height is 570/1.65 = 5.75 min (~6 min). This time is far greater than the advective time scale (wind speed) at the location. For island surface
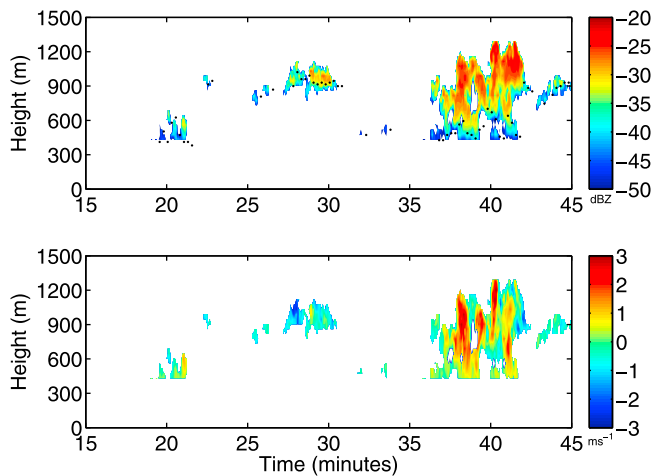
Figure 2. Sample 30 min period showing the (top) reflectivity and (bottom) mean Doppler velocity as observed by WACR at the AMF. The ceilometer observed first cloud base height is also shown in Figure 2 (top). Positive Doppler velocity denotes updrafts, while negative Doppler velocity denotes downdrafts. There were a total of nine cloud elements determined during this time.

eddies to reach the cumulus cloud base height within the first 100 m of the island will need a wind speed of 0.3 m s^{-1}, while the average wind speed was 4.55 m s^{-1}. Although some effect of island heating on the observed clouds cannot be ruled out, it is safe to assume that most of the sampled clouds were of undisturbed marine origin.

[9] A sample 30 min period of fair weather cumulus clouds as observed by the WACR on 26 June 2009 is shown in Figure 2 along with the ceilometer observed first cloud base height. The forced, active, and passive stages of cumulus as described by *Stull* [1985] are present during this time period. These stages are identified by their updraft structure and location relative the LCL. The radiosondes launched during this period did not record any significant change in horizontal wind direction with height, suggesting a smaller probability for the radar to miss the clouds or observe just the cloud edges, but the possibility cannot be ruled out completely. The radar was able to observe the thin clouds (30–35 min) whose presence was confirmed by the ceilometer. The forced clouds (18–22 min), passive clouds (25–30 min) and active clouds (36–43 min) had reflectivity less than −20 dBZ suggesting absence of any precipitation size droplets [*Feingold et al.*, 1999]. Cloud droplets have negligible fall velocity and are transported by the BL turbulent eddies. Doppler velocity as observed by zenith pointing radar can be used as a surrogate for vertical air motion in the absence of precipitation [e.g., *Frisch et al.*, 1995; *Ghate et al.*, 2010]. Different stages of cumulus have comparable reflectivity, but differ in their dynamic structure as seen through the mean Doppler velocity (Figure 2, bottom). Forced clouds are characterized by weak updrafts, passive clouds predominantly with downdrafts, and active clouds with multiple updraft cores analogous to as proposed by *Stull* [1985]. A cloud masking algorithm was developed from the reflectivity data similar to that by *Clothiaux et al.*

[2000] to assist in the identification and classification of individual cloud elements.

3. General Conditions

[10] Fair weather cumulus clouds were observed in a range of conditions as tabulated in Table 1. All periods with BL trade cumulus clouds observed for more than three consecutive hours were chosen for analysis, with none of the data that matched this criteria were rejected. A precipitation event with precipitation originating from higher level clouds forced the separation of data from 15 September 2009 into two separate cases that exhibited different BL structure. The general conditions observed during marine trade wind BL are tabulated in Tables 1 and 2. The tabulated values are averages for the entire duration of case which were calculated from the hourly averages. The surface wind speed varied between 2.78 m s^{-1} to 6.40 m s^{-1}. The contribution of surface buoyancy to the BL turbulence is quantified using the surface convective velocity scale (w*) and for the cases examined here it varied from 0.05 m s^{-1} to 0.6 m s^{-1}. This range suggests that some of the observed cumuli (especially during low w* conditions) might result from shear induced BL turbulence or cloud top radiative cooling. The ECMWF model simulated large-scale vertical velocity (subsidence) varied from about 30 to 150 mbar d^{-1} during the events. Inversion strength was quantified by the gradient of potential temperature and mixing ratio across the inversion. The average potential temperature and mixing ratio gradients for the cases calculated from the launched radiosondes are reported in Table 1. The inversion capping the BL was as strong as 7.16 k (20090615) and 6.44 gkg^{-1} (20090606) and was absent during other cases (20090626, 20091016 and 20091017). The vertical shear of horizontal velocity within the cloud layer [*Lemone*, 1989] which is sum of the squares of difference between the wind speed components near cloud base and near cloud top divided by the cloud thickness was calculated for each sounding. The wind shear contribution to the BL turbulence did not exhibit large variation and ranged from 0.42 to 17.93 × 10^{-3} s^{-1}, which is consistent with the results of *Lemone* [1989]. The surface aerosol concentration as measured by the CPC varied from 505 to 1066 cm^{-3}. Some unusually high values of aerosol concentration were observed and discarded after it was determined that they corresponded to ship tracks or other anthropogenic source.

[11] A total of 557 individual cloud elements were observed. The lowest ceilometer observed hourly cloud cover was 5% while the highest was 84%. The ceilometer observed hourly cloud cover averaged for individual cases ranged from 20 to 40% (Table 2). The case mean cloud top height varied from 472 to 946 m, while the case mean cloud base height varied from 350 m to 830 m. The average coefficient of variation defined as the ratio of standard deviation to the mean value was 0.17 for both the cloud base height and cloud top height, which stated another way is approximately 20%.

[12] The shallowness of these clouds, which had depths ranging from 121 to 193 m, suggests that they are predominantly of the forced genera rather than fully developed active cumuli. This shallowness emphasizes the need to observe them with higher sensitive radars operating at a

Table 2. Cloud Conditions During the Cases[a]

Date (yyyymmdd)	Number of Clouds	Ceilometer Cloud Cover (%)	Cloud Top Height (m)		Cloud Base Height (m)		Cloud Depth (m)		Cloud Chord Length (m)	
			Mean	Std	Mean	Std	Mean	Std	Mean	Std
20090606	53	24.36	696	141	542	109	153	98	475	371
20090615	49	20.38	946	115	830	111	115	50	381	240
20090626	63	27.13	669	114	526	79	142	84	593	456
20090712	65	19.44	863	80	731	48	131	71	437	321
20090915a	108	43.67	785	176	592	119	193	114	757	1003
20090915b	50	27.05	872	142	709	84	162	108	525	432
20091016	72	44.85	504	97	349	50	154	75	524	420
20091017	50	31.36	472	92	350	57	121	64	377	247
20091019	57	34.02	621	146	490	96	131	83	486	522

[a]Columns represent date, number of clouds, mean hourly ceilometer reported cloud cover, mean and standard deviation of cloud top height, cloud base height, cloud depth and cloud chord length. For dates, yyyymmdd denotes year, month, and day; read 20090615 as 15 June 2009. Presented values are case means calculated form hourly averages.

finer range resolution, such as the radar used in this study. The average coefficient of variation for cloud depth was 0.55, which is higher than that of cloud top height and cloud base height. This is mainly due to the lower mean value of cloud depth, rather than higher variance. The cloud chord length was also determined by multiplying the amount of time the cloud element was observed over the radar with the average surface wind speed during that time [*Berg and Kassianov*, 2008]. It varied from 377 m to 757 m, with some clouds having length of more than a kilometer. The clouds with longer than a kilometer chord length might be transitioning from cumulus to stratocumulus, but nevertheless most of the clouds had chord lengths under 500 m. Scatterplots between cloud depth and cloud chord length (not shown) yielded no statistically significant relationship. The coefficient of variation for cloud chord length was about 0.84 with the standard deviation being greater than the mean value during one case (20090915a).

[13] Generating ensemble statistics in a manner preserving the identity of forced, active and passive clouds required that the height be normalized by the maximum cloud top height (z_t) and minimum cloud base height (z_b) observed during any particular case. The cloud layer depth normalized height (η) at any height z was calculated as

$$\eta = \frac{z - z_b}{z_t - z_b}.$$

Boundary layer evolution was present in a few cases and the BL height increased with commensurate increases in the cloud top height and cloud base height, but these changes are well characterized by the normalization procedure. The observed radar samples were also tagged as "core" samples when the vertical velocity was positive and "coherent" when the vertical velocity was positive in the entire cloud layer. Histograms of reflectivity at four cloud depth normalized levels are shown in Figure 3. None of the reflectivity values exceeded the threshold value of −20 dBZ at any level, reaffirming the absence of precipitation size hydrometeors. Mean reflectivity increased from −37 dBZ at $\eta = 0.2$ to −28 dBZ at $\eta = 0.8$ in a manner that is consistent with higher liquid water content and larger cloud drops near cloud top, while the mean reflectivity of core and coherent samples did not differ significantly from that calculated from all samples. Mean reflectivity is observed to increase rapidly in the lower

half of the clouds relative to the upper half and the distribution of reflectivity narrows sharply in the vicinity of cloud top as indicated by increased kurtosis.

[14] Histograms of vertical velocity at four normalized cloud depths are shown in Figure 4 and positive vertical velocities indicate updrafts. Mean vertical velocity from all levels remained approximately constant at ∼0.33 m s^{-1} through the entire clouds, although there is a slight increase at $\eta = 0.4$. The width of the probability distribution function of the "all" and "coherent" samples increased linearly from cloud base till cloud top reflecting more turbulent conditions
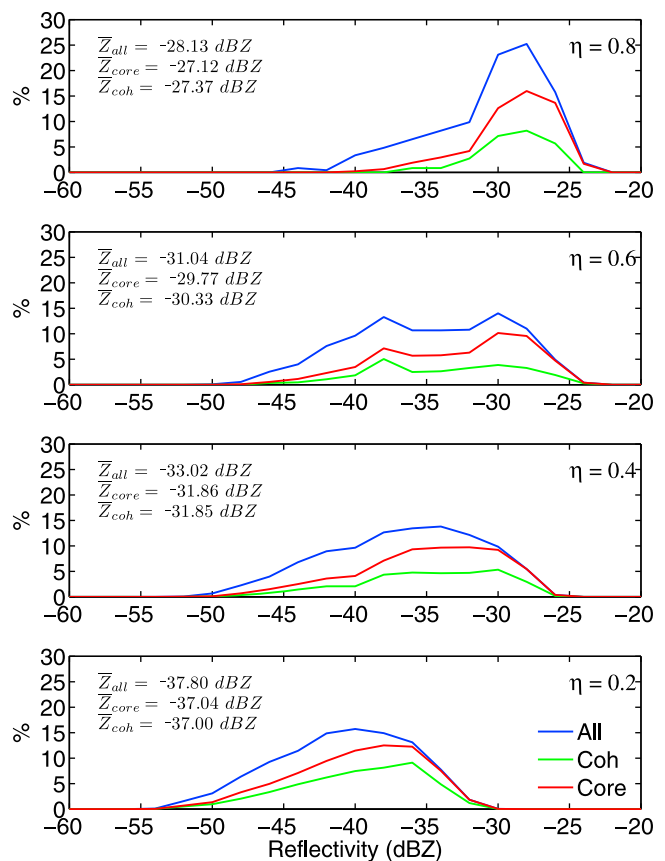

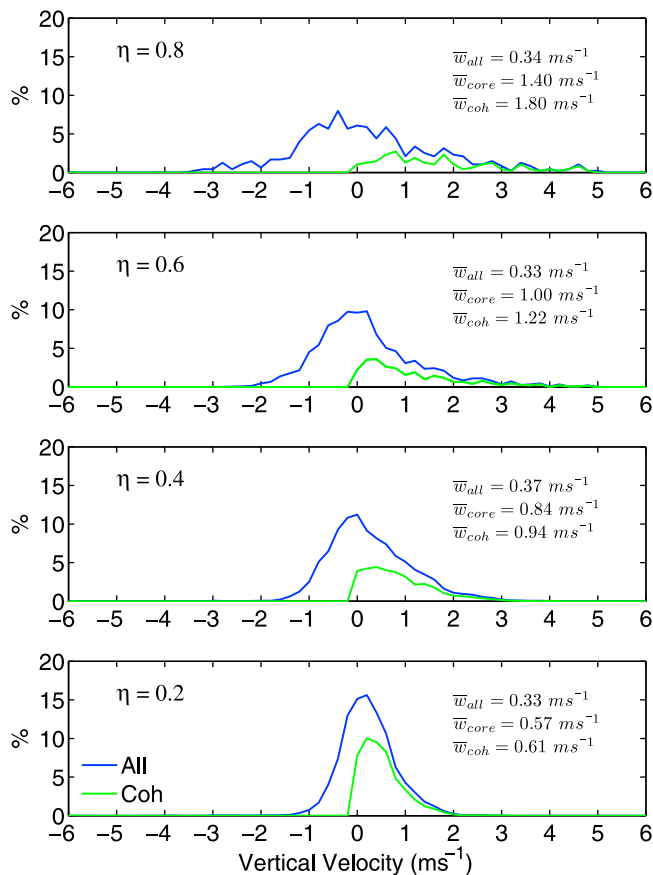**Figure 3.** Histogram of reflectivity at four BL depth normalized levels for all, core, and coherent samples.

Figure 4. Histogram of vertical velocity at four BL depth normalized levels (η). The mean of the distribution is also reported in each panel.

near cloud top. Maximum updraft velocity reached 5 m s^{-1} and the maximum downdraft velocity was −3.5 m s^{-1}. These values are less than the maximum unambiguous velocity that could be observed by the WACR, which is 8 m s^{-1}. Progressing upward from cloud base the mean velocity of the core and coherent samples are observed to increase over twofold, with the highest incremental increase from $\eta = 0.6$ to $\eta = 0.8$. This may be a result of the conversion of CAPE to kinetic energy (KE) by the active clouds.

[15] Although the coherency test does not account for any tilt in the updrafts, the difference between the wind direction near cloud top and near cloud base did not exceed 30° for any soundings, with most of them being lower than 10°. Also, the wind shear within the cloud layer was small (Table 1). Most of the updrafts greater than 0.5 m s^{-1} at $\eta = 0.2$ were coherent, while almost all the updrafts greater than 1 m s^{-1} at $\eta = 0.8$ were coherent. In other words, coherent updrafts are associated with greater than average vertical velocities at the cloud boundaries (cloud base and cloud top). Strong thermals at cloud base and significant turbulent mixing at cloud top would be implicated as mechanisms associated with coherent vertical velocity profiles in these trade cumulus clouds. When the hourly mean vertical velocity of the coherent and core samples are compared at different levels the difference between them is seen to gradually increase from 0.04 m s^{-1} at $\eta = 0.2$ to 0.4 m s^{-1} near cloud top. This structural difference suggests that secondary circulations are present near cloud

top, which generate local updrafts that do not span the entire cloud layer.

[16] The cloud mass flux (F_i) was also calculated following the classic plume decomposition approach [Arakawa, 2004] using the mean vertical velocity (w_i) and the fractional coverage of vertical velocity (σ_i) for velocities between −5 m s^{-1} to 5 m s^{-1} with bins centered at 0.1 m s^{-1} interval and having the same width. Fraction is calculated with respect to total number of radar samples collected during an hour and the mass flux is written as

$$F_i = \rho_{air} \, w_i \, \sigma_i$$

where the density of air (ρ_{air}) is assumed to be constant at 1.2 kg m^{-3} and subscript i refers to the velocity bin. Traditionally, the definition of the mass flux requires that the mean velocity be subtracted from the instantaneous velocities. Since the radar can only observe cloudy portion of the BL it is assumed that downdrafts in a fair weather BL occur between cloud elements and that the mean vertical velocity at each level on hourly time scales is zero. Also, the large-scale vertical velocities from the ECMWF model at the cloud heights are less than a 0.01 m s^{-1} suggesting that the neglect of the mean velocity is not a serious limitation to the calculation of mass flux. Mass flux estimates using this approach are impacted by increases in the BL depth (inversion base height) although a 100 m increase in BL depth in an hour corresponds to a mean velocity of 0.02 m s^{-1}, which is negligible in comparison to the vertical velocities observed in these clouds. The BL depth did not increase by more than 100 m during any hour, so the mean vertical velocity on hourly time scales is assumed to be zero.

[17] Mass fluxes binned according to vertical velocity at four normalized depths in these trade cumulus clouds are shown in Figure 5. These data are further sorted by updraft mass flux and the mass flux contribution from coherent samples. Although higher velocities are observed near cloud top most of the mass transport is in the lower half of the cloud, which is primarily due to higher updraft fractions in the lower half of the clouds. The updraft mass flux decreases from ~22 g^{-2} s^{-1} to 4 g^{-2} s^{-1} from cloud base to top, so the updraft mass flux at $\eta = 0.8$ is only ~13% of that at $\eta = 0.2$. This structural alignment results from more vigorous updrafts in the upper half of the clouds that cover a smaller fraction of area, so the total mass transport is small. The average contribution of coherent mass flux to the total updraft mass flux is ~62% suggesting that coherent updrafts are not dominant transporters of mass, but carry a slightly larger portion than other updraft configurations. Cloudy portions of the BL are assumed to be associated with rising thermals and hence updraft mass fluxes, but the WACR recorded significant downdraft mass fluxes embedded within these thermals.

[18] The hourly averaged reflectivity, vertical velocity, fraction and mass flux from all, core and coherent samples is shown in Figure 6. The averaged reflectivity did not exhibit any changes between all, core and coherent samples on hourly time scales. Adiabatic cloud models contain only a quiescent rising thermal and indicate that the radar reflectivity and LWC increase from cloud base to top. The LWC profile is expected to be adiabatic in coherent samples, near adiabatic in core samples and subadiabatic in all samples. Since, the reflectivity is proportional to the sixth moment of the
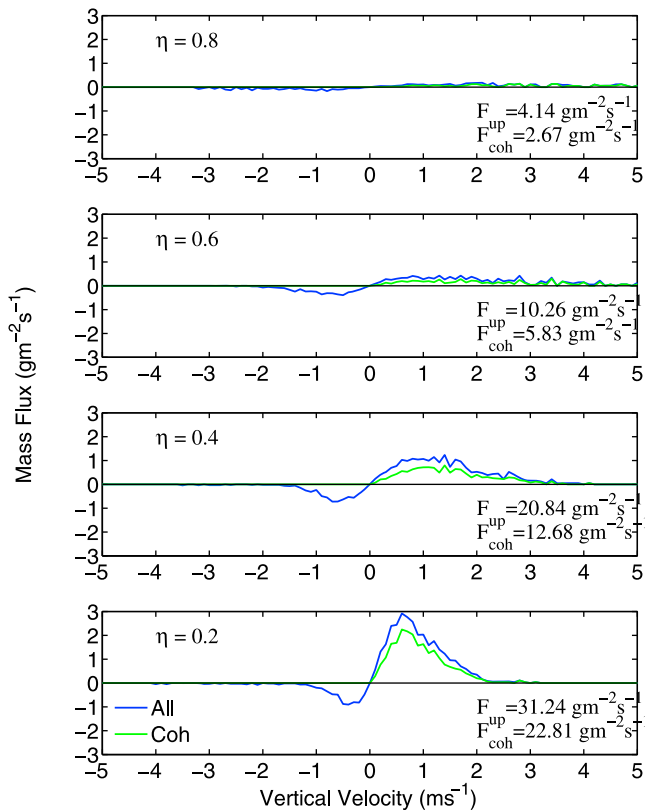
Figure 5. Velocity binned mass flux from all and coherent samples at four BL depth normalized levels. The updraft mass flux at each level is also reported.

drop size distribution, similar reflectivity profiles of all, core and coherent samples suggest that the evaporation of the small drops caused by the mixing associated with the downdrafts might have impact on the LWC but does not cause any changes in the reflectivity.

[19] Average vertical velocity from all the cloudy samples is almost constant throughout the cloud layer at ~0.3 m s^{-1}, while core and coherent samples increased with height. The maximum velocity of the core samples was 1.5 m s^{-1} and that of coherent samples 2.5 m s^{-1} and the maximum velocity was observed near cloud top in both instances. This structural configuration is consistent with model simulations shown by *Golaz et al.* [2005] and *Siebesma et al.* [2003]. The configurations of the "all" and "core" fractions are particularly similar to those reported by *Siebesma et al.* [2003] simulating a case from the BOMEX (Barbados Oceanographic and Meteorological Experiment). The "all" and "core" fractions in that study [*Siebesma et al.*, 2003] were about 5.5% and 3.5% near cloud base and decreased above that. It should be noted that in this study, updrafts which are vertically coherent in the entire cloud layer have been termed as "core" samples, while in the study by *Siebesma et al.* [2003] updrafts with positive liquid water content and a positive buoyancy flux have been termed as "core" samples.

[20] The hourly averaged mass flux was about 0.03 kg m^2 s^{-1} near cloud base for all samples. Downdrafts contribute negative mass flux by definition and the mass flux of all

samples is lower than that of the coherent samples, which is expected. Although the fraction of the core samples is lower than that of all samples, due to higher velocity of the core samples, the mass flux contribution of all and coherent samples is similar (~0.025 m s^{-1}) near cloud base. Partly due to lower fraction and downdrafts present near cloud top, the mass flux contribution from all samples is lower than that of coherent samples near cloud top.

[21] To statistically quantify the vertical velocity structure of these clouds, the variance, skewness, updraft and downdraft fraction was calculated for each hour (Figure 7). The updraft and downdraft fraction were also conditionally sampled for six different vertical velocity thresholds. The magnitudes of these thresholds are shown in Figure 7d, while the thresholds are positive for updrafts and negative for downdrafts. Since, the radar can only observe the cloudy portion of the BL, the reported variances and skewness are the contribution of the observed vertical velocity to the total BL variance and skewness and cannot be compared directly to results from past studies. Similar to the calculation of mass flux, the hourly average vertical velocity within the BL was assumed to be zero. Hence, the reported vertical velocity variance is the sum of the square of the observed (cloudy) vertical velocities divided by the total number of samples (cloud + noncloudy) in one hour as observed by the radar.

[22] The contribution of the observed vertical velocity variance to the total BL variance is ~0.03 m^2 s^{-2} near cloud base and decreases toward cloud top. Variance contributions from core samples is 0.028 m^2 s^{-2} and the variance from coherent samples is 0.022 m^2 s^{-2} near cloud base. Decreasing variance contribution with height is a result of decreased cloud fraction at the higher levels. Observed vertical velocity skewness decreased from 5 near cloud base to 1 at $\eta = 0.7$, and showed a zig-zag structure above, while the skewness contribution from coherent and core samples increased upward in the cloud from ~7 near cloud base to ~16 near cloud top. Previous modeling studies based on
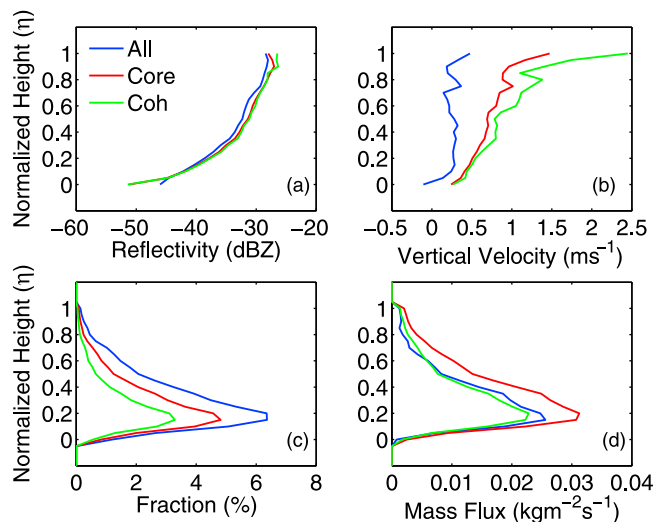

Figure 6. BL depth normalized profiles of hourly averaged (a) reflectivity, (b) vertical velocity, (c) fraction, and (d) mass flux for all, core, and vertically coherent updraft samples.
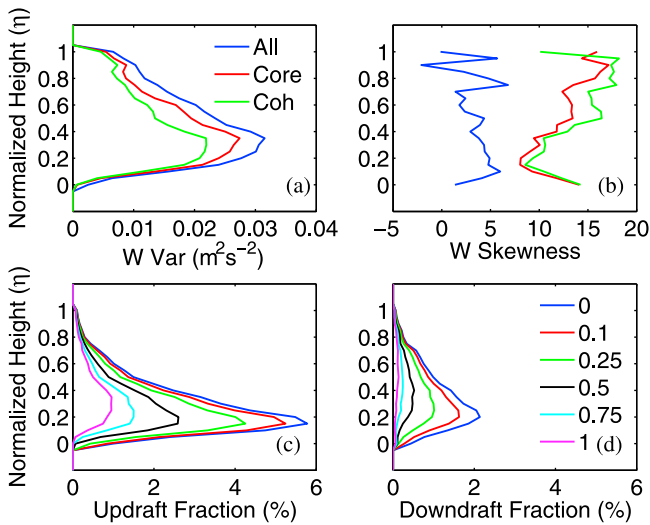
Figure 7. BL depth normalized profile of hourly averaged (a) contribution of all, core, and coherent samples to total w variance, (b) vertical velocity skewness of all, core, and coherent samples, (c) conditionally sampled in-cloud updraft fraction, and (d) conditionally sampled in-cloud downdraft fraction. The legends for curves in Figures 7a and 7b are shown in Figure 7a, while those in Figures 7c and 7d are shown in Figure 7d.

LES simulations project that the total BL vertical velocity variance and skewness increase with height from cloud base to cloud top with a variance near cloud top of approximately 0.1 m^2 s^{-2} [*Siebesma et al.*, 2003] and skewness near cloud top around ~4.5 [*Golaz et al.*, 2005; *Zhu and Zuidema*, 2009].

[23] Updraft fraction was about 6% near cloud base with a decrease above that, while the downdraft fraction was about 2% near cloud base and also decreased upward in the clouds. The maxima of the conditionally sampled updraft or downdraft fraction is higher within the cloud layer for higher thresholds, with the fraction of updrafts greater than 1 m s^{-1} being constant from $\eta = 0.2$ to $\eta = 0.4$. The fraction of downdrafts stronger than -1 m s^{-1} increased from cloud base till middle of the cloud and then decreased upward in the cloud. For similar thresholds the downdraft fractions did not exhibit a sharp peak as the updraft fractions.

4. Vertical Velocity Variability

[24] To further characterize the vertical velocity structure of these clouds, the hourly statistics were classified into different categories based on the surface convective velocity scale, radiative heating, shear etc. The hourly profiles when classified based on BL radiative heating (similar to day and night) or shear within the cloud layer showed no significant response and are not discussed. Mean reflectivity, vertical velocity, cloud fraction and mass flux as contributed by core samples for the classification based on the ECMWF model reported w* are analyzed below.

[25] To assess the impact of subcloud turbulence on the in-cloud turbulence, the observed data were classified based on the ECMWF model reported w*. Nineteen hours had w*

less than 0.2 m s^{-1} while 17 h had w* greater than 0.6 m s^{-1}. The average w* for hours with w* less than 0.2 m s^{-1} was 0.02 m s^{-1} while the average w* for hours with w* greater than 0.6 m s^{-1} was 0.64 m s^{-1}. The mean cloud base height and cloud top height during hours with w* less than 0.2 m s^{-1} was 463 m and 849.72 m respectively, while the same during hours with w* greater than 0.6 m s^{-1} was 550.92 m and 1080.3 m respectively. Hence, the cloud layer height was higher during hours with w* greater than 0.6 m s^{-1} compared to that during hours with w* less than 0.2 m s^{-1}. Also, the cloud layer thickness was greater during hours with w* greater than 0.6 m s^{-1} than during hours with w* less than 0.2 m s^{-1}. The standard deviation of cloud base height, cloud top height and cloud thickness during hours with w* less than 0.2 m s^{-1} was 180 m, 199 m and 159 m respectively, while the same during hours with w* greater than 0.6 m s^{-1} was 67 m, 334 m and 365 m respectively.

[26] The profiles of average reflectivity, core vertical velocity, cloud fraction and mass flux for this classification are shown in Figure 8. The average reflectivity during hours with w* greater than 0.6 m s^{-1} was greater than that during hours with w* less than 0.2 m s^{-1} in the entire cloud layer. The difference between the average reflectivity during hours with w* less than 0.2 m s^{-1} and during hours with w* greater than 0.6 m s^{-1} was negligible near cloud base. The difference was ~5 dBZ at $\eta = 0.7$ and ~3 dBZ near cloud top. The average vertical velocity during hours with w* less than 0.2 m s^{-1} was lower than those with w* greater than 0.6 m s^{-1} in the entire cloud layer except at $\eta = 0.8$, where both were equal. The difference between the two was greatest in the middle of the cloud layer. The average cloud fraction near cloud base for hours with w* less than 0.2 m s^{-1} was 6.22% while the same for hours with w* greater than 0.6 m s^{-1} was 9.5%. The standard deviation of the cloud fraction at cloud base was 3.9% and 8% for
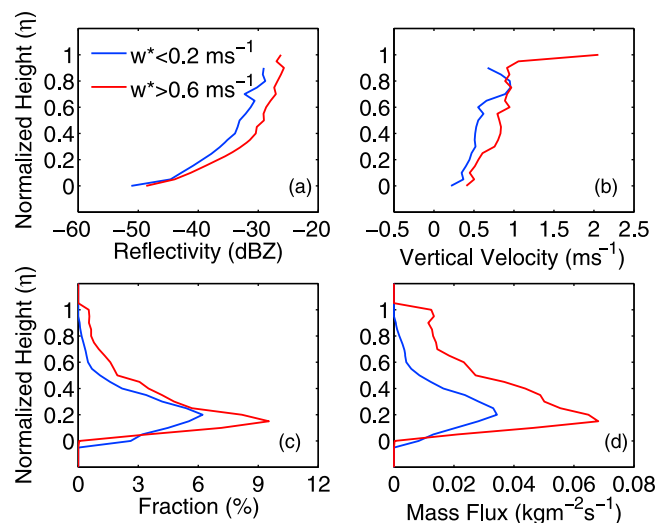

Figure 8. Mean cloud layer depth normalized profiles of (a) reflectivity, (b) vertical velocity, (c) fraction, and (d) mass flux for hours when surface convective velocity scale was less than 0.2 m s^{-1} and for hours when it was greater than 0.6 m s^{-1}. Profiles shown are for the core samples only.
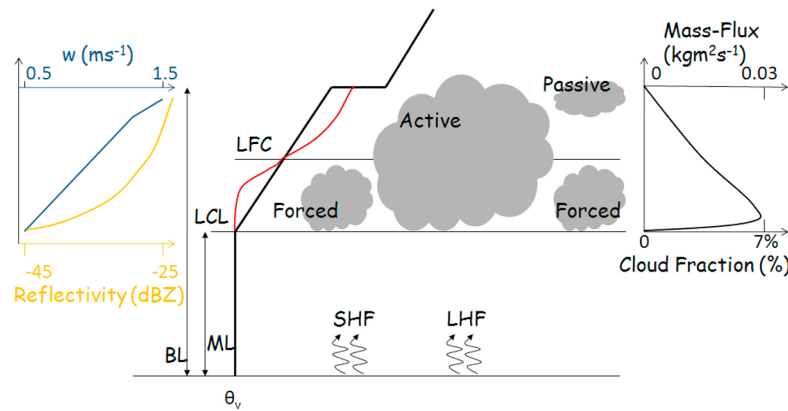
Figure 9. Schematic diagram showing the general conditions associated with a fair weather boundary layer. SHF, sensible heat flux; LHF, latent heat flux; LCL, lifting condensation level; LFC, level of free convection; ML, mixed layer.

hours with w* less than 0.2 m s^{-1} and hours with w* greater than 0.6 m s^{-1} respectively. The average mass flux near cloud base during hours with w* less than 0.2 m s^{-1} was 0.034 kg m^{-2} s^{-1}, while the same during hours with w* greater than 0.6 m s^{-1} was 0.068 kg m^{-2} s^{-1}. The standard deviation of mass flux near cloud base was 0.025 kg m^{-2} s^{-1} and 0.075 kg m^{-2} s^{-1} for hours with w* less than 0.2 m s^{-1} and hours with w* greater than 0.6 m s^{-1} respectively. The cloud fraction near cloud base during hours with w* greater than 0.6 m s^{-1} was almost 150% to that during hours with w* less than 0.2 m s^{-1}, while the mass flux near cloud base during hours with w* greater than 0.6 m s^{-1} was almost 200% to that observed during hours with w* less than 0.2 m s^{-1}. The differences between the mass flux and cloud fraction at levels above $\eta = 0.6$ suggests that clouds of active genera were more prevalent during hours with w* greater than 0.6 m s^{-1} than during hours with w* less than 0.2 m s^{-1}.

5. Summary and Discussion

[27] Oceanic trade wind cumulus clouds are an important component of the Earth's radiation budget and the general circulation of the atmosphere. They regulate the throughput of solar radiation and the transport of water vapor from the marine boundary layer into the free troposphere in the tropics. Remote sensors deployed on the island of Graciosa, Azores, which lies in the central Atlantic Ocean, enabled the dynamical structure of 557 individual oceanic trade cumulus elements to be analyzed. The absence of sea surface flux measurements to accompany the cloud observations necessitated the use of ECMWF simulated fluxes and surface meteorology.

[28] The oceanic trade cumulus BL is generally associated with weak but persistent surface turbulent heat fluxes (SHF and LHF) with an embedded cloud layer that is thermodynamically sometimes decoupled from surface forcing. A composite representation of the conditions observed during this study schematic depicting the general conditions in trade wind BL is shown in Figure 9. The cloud base height of the forced and active clouds matches the LCL, which is also the

top of the mixed layer. The environmental profile of virtual potential temperature exhibits a inversion at the top of the BL capping the cloud layer. The red line denotes the profile of a parcel lifted from the surface layer adiabatically till the BL inversion base. The thermals associated with the active clouds have enough inertia to penetrate through the Convective Inhibition Energy (CIN) to reach the top of the mixed layer and utilize the Convective Available Potential Energy (CAPE), while the forced clouds fail to do so. The reflectivity increases with height from cloud base till cloud top while the velocity increases almost linearly from cloud base till cloud top with the slope being greater when the parcel overcome CIN and is warmer than the environment (CAPE region). The cloud fraction and mass flux exhibit similar profiles, which is indicative of the domination of forced clouds. The numbers presented in the schematic pertain to the updraft-only (core) samples. The observed hourly values were classified based on the surface convective velocity scale as reported by the ECMWF model. The cloud fraction near cloud base during hours with w* greater than 0.6 m s^{-1} was 150% of that observed during hours with w* less than 0.2 m s^{-1}. While the mass flux near cloud base during hours with w* greater than 0.6 m s^{-1} was 200% of that observed during hours with w* less than 0.2 m s^{-1}.

[29] Some of the existing instrumentation (e.g., microwave radiometer, soundings) is not able to accurately observe the meteorology under their current operating setups due to challenges presented by the broken cloud field. Because of high variability in the BL thermodynamic structure in a broken cloud field, it is necessary to either launch the soundings at a higher temporal resolution or to develop new instruments which could observe the BL thermodynamic structure at a temporal and spatial resolution finer than the cloud field inhomogeneity. The same applies for the microwave radiometer, which yields the liquid water path associated with the cumulus cloud field. A cloud radar can yield only the dynamical structure of the cloudy portion of the BL, while in the fair weather BL, the cloud fraction is low (~25%) leaving a larger portion of clear air BL. A complimentary vertically pointing Doppler lidar together

with the Doppler radar will yield the dynamical structure of the entire BL in all conditions.

References

Albrecht, B. A. (1981), Parameterization of trade-cumulus cloud amounts, *J. Atmos. Sci.*, *38*, 97–105, doi:10.1175/1520-0469(1981)038<0097:POTCCA>2.0.CO;2.

Albrecht, B., M. Jensen, and W. Syrett (1995a), Marine boundary layer structure and fractional cloudiness, *J. Geophys. Res.*, *100*(D7), 14,209–14,222, doi:10.1029/95JD00827.

Albrecht, B. A., C. S. Bretherton, D. Johnson, W. H. Scubert, and A. S. Frisch (1995b), The Atlantic Stratocumulus Transition Experiment—ASTEX, *Bull. Am. Meteorol. Soc.*, *76*, 889–904, doi:10.1175/1520-0477(1995)076<0889:TASTE>2.0.CO;2.

Arakawa, A. (2004), The cumulus parameterization problem: Past, present and future, *J. Clim.*, *17*, 2493–2525, doi:10.1175/1520-0442(2004)017<2493:RATCPP>2.0.CO;2.

Augstein, E., H. Riehl, F. Ostapoff, and V. Wagner (1973), Mass and energy transports in an undisturbed Atlantic trade-wind flow, *Mon. Weather Rev.*, *101*, 101–111, doi:10.1175/1520-0493(1973)101<0101:MAETIA>2.3.CO;2.

Berg, L. K., and E. I. Kassianov (2008), Temporal variability of fair-weather cumulus statistics at the ACRF SGP site, *J. Clim.*, *21*, 3344–3358, doi:10.1175/2007JCLI2266.1.

Berg, L. K., and R. B. Stull (2005), A simple parameterization coupling the convective daytime boundary layer and fair-weather cumuli, *J. Atmos. Sci.*, *62*, 1976–1988, doi:10.1175/JAS3437.1.

Berg, L. K., et al. (2009), Overview of the Cumulus Humilis Aerosol Processing Study (CHAPS), *Bull. Am. Meteorol. Soc.*, *90*, 1653–1667, doi:10.1175/2009BAMS2760.1.

Bretherton, C. S., J. R. McCaa, and H. Grenier (2004), A new parameterization for shallow cumulus convection and its application to marine subtropical cloud-topped boundary layers. Part I: Description and 1D results, *Mon. Weather Rev.*, *132*, 864–882, doi:10.1175/1520-0493(2004)132<0864:ANPFSC>2.0.CO;2.

Brown, A. R., et al. (2002), Large-eddy simulation of the diurnal cycle of shallow cumulus convection over land, *Q. J. R. Meteorol. Soc.*, *128*, 1075–1093, doi:10.1256/003590002320373210.

Clothiaux, E. E., T. P. Ackerman, G. G. Mace, K. P. Moran, R. T. Marchand, M. A. Miller, and B. E. Martner (2000), Objective determination of cloud heights and radar reflectivities using a combination of active remote sensors at the ARM CART sites, *J. Appl. Meteorol.*, *39*, 645–665, doi:10.1175/1520-0450(2000)039<0645:ODOCHA>2.0.CO;2.

Feingold, G., A. S. Frisch, B. Stevens, and W. R. Cotton (1999), On the relationship among cloud turbulence, droplet formation and drizzle as viewed by Doppler radar, microwave radiometer and lidar, *J. Geophys. Res.*, *104*(D18), 22,195–22,203, doi:10.1029/1999JD900482.

Frisch, A. S., D. H. Lenschow, C. W. Fairall, W. H. Schubert, and J. S. Gibson (1995), Doppler radar measurements of turbulence in marine stratiform clouds during ASTEX, *J. Atmos. Sci.*, *52*, 2800–2808, doi:10.1175/1520-0469(1995)052<2800:DRMOTI>2.0.CO;2.

Ghate, V. P., B. A. Albrecht, and P. Kollias (2010), Vertical velocity structure of nonprecipitating continental boundary layer stratocumulus clouds, *J. Geophys. Res.*, *115*, D13204, doi:10.1029/2009JD013091.

Golaz, J.-C., V. E. Larson, and W. R. Cotton (2002), A pdf-based model for boundary layer clouds. Part I: Method and model description, *J. Atmos. Sci.*, *59*, 3540–3551, doi:10.1175/1520-0469(2002)059<3540:APBMFB>2.0.CO;2.

Golaz, J. C., S. Wang, J. D. Doyle, and J. M. Schmidt (2005), COAMPS®-Les: Model evaluation and analysis of second-and third-moment vertical velocity budgets, *Boundary Layer Meteorol.*, *116*, 487–517, doi:10.1007/s10546-004-7300-5.

Grant, A. L. M. (2001), Cloud-base fluxes in the cumulus-capped boundary layer, *Q. J. R. Meteorol. Soc.*, *127*, 407–421, doi:10.1002/qj.49712757209.

Jiang, H., H. Xue, A. Teller, G. Feingold, and Z. Levin (2006), Aerosols effects on lifetime on shallow cumulus, *Geophys. Res. Lett.*, *33*, L14806, doi:10.1029/2006GL026024.

Jiang, H., G. Feingold, and I. Koren (2009), Effect of aerosol on trade cumulus cloud morphology, *J. Geophys. Res.*, *114*, D11209, doi:10.1029/2009JD011750.

Kollias, P., and B. Albrecht (2010), Vertical velocity statistics in fair-weather cumuli at the ARM TWP Nauru climate research facility, *J. Clim.*, *23*, 6590–6604, doi:10.1175/2010JCLI3449.1.

Koren, I., G. Feingold, H. Jiang, and O. Altaratz (2009), Aerosol effects on the intercloud region of a small cumulus cloud field, *Geophys. Res. Lett.*, *36*, L14805, doi:10.1029/2009GL037424.

Lappen, C.-L., and D. A. Randall (2001), Toward a unified parameterization of the boundary layer and moist convection. Part I: A new type of mass-flux model, *J. Atmos. Sci.*, *58*, 2021–2036, doi:10.1175/1520-0469(2001)058<2021:TAUPOT>2.0.CO;2.

Lemone, M. A. (1989), The influence of vertical wind shear on the diameter of cumulus clouds in CCOPE, *Mon. Weather Rev.*, *117*, 1480–1491, doi:10.1175/1520-0493(1989)117<1480:TIOVWS>2.0.CO;2.

Neggers, R. A. J. (2009), A dual mass flux framework for boundary layer convection. Part II: Clouds, *J. Atmos. Sci.*, *66*, 1489–1506, doi:10.1175/2008JAS2636.1.

Neggers, R. A. J., H. J. J. Jonker, and A. P. Siebesma (2003), Size statistics of cumulus cloud populations in large-eddy simulations, *J. Atmos. Sci.*, *60*, 1060–1074, doi:10.1175/1520-0469(2003)60<1060:SSOCCP>2.0.CO;2.

Neggers, R., J. D. Neelin, and B. Stevens (2007), Impact mechanisms of shallow cumulus convection on tropical climate dynamics, *J. Clim.*, *20*, 2623–2642, doi:10.1175/JCLI4079.1.

Rauber, R. M., et al. (2007), Rain in shallow cumulus over the ocean: The RICO campaign, *Bull. Am. Meteorol. Soc.*, *88*, 1912–1928, doi:10.1175/bams-88-12-1912.

Rodts, S. M. A., P. G. Duynkerke, and H. J. J. Jonker (2003), Size distributions and dynamical properties of shallow cumulus clouds from aircraft observations and satellite data, *J. Atmos. Sci.*, *60*, 1895–1912, doi:10.1175/1520-0469(2003)060<1895:SDADPO>2.0.CO;2.

Siebesma, A. P., and J. W. M. Cuijpers (1995), Evaluation of parametric assumptions for shallow cumulus convection, *J. Atmos. Sci.*, *52*, 650–666, doi:10.1175/1520-0469(1995)052<0650:EOPAFS>2.0.CO;2.

Siebesma, A. P., et al. (2003), A large eddy simulation intercomparison study of shallow cumulus convection, *J. Atmos. Sci.*, *60*, 1201–1219, doi:10.1175/1520-0469(2003)60<1201:ALESIS>2.0.CO;2.

Stevens, B., et al. (2001), Simulations of trade wind cumuli under a strong inversion, *J. Atmos. Sci.*, *58*, 1870–1891, doi:10.1175/1520-0469(2001)058<1870:SOTWCU>2.0.CO;2.

Stull, R. B. (1985), A fair-weather cumulus cloud classification scheme for mixed-layer studies, *J. Clim. Appl. Meteorol.*, *24*, 49–56, doi:10.1175/1520-0450(1985)024<0049:AFWCCC>2.0.CO;2.

Tiedtke, M., W. A. Heckley, and J. Slingo (1988), Tropical forecasting at ECMWF: The influence of physical parameterizations on the mean structure of forecasts and analyses, *Q. J. R. Meteorol. Soc.*, *114*, 639–665, doi:10.1256/smsqj.48105.

von Salzen, K., and N. A. McFarlane (2002), Parameterization of the bulk effects of lateral and cloud-top entrainment in transient shallow cumulus clouds, *J. Atmos. Sci.*, *59*, 1405–1430, doi:10.1175/1520-0469(2002)059<1405:POTBEO>2.0.CO;2.

Warren, S. G., C. J. Hahn, J. London, R. M. Chervin, and R. L. Jenne (1988), Global distribution of total cloud cover and cloud type amounts over the ocean, *NCAR Tech. Note TN-317+STR*, 42 pp. + 170 maps, NCAR, Boulder, Colo.

Zhu, P., and B. Albrecht (2002), A theoretical and observational analysis on the formation of fair-weather cumuli, *J. Atmos. Sci.*, *59*, 1983–2005, doi:10.1175/1520-0469(2002)059<1983:ATAOAO>2.0.CO;2.

Zhu, P., and P. Zuidema (2009), On the use of PDF schemes to parameterize sub-grid clouds, *Geophys. Res. Lett.*, *36*, L05807, doi:10.1029/2008GL036817.

V. P. Ghate, M. A. Miller, and L. DiPretore, Department of Environmental Sciences, Rutgers University, 14 College Farm Rd., New Brunswick, NJ 08901, USA. (vghate@envsci.rutgers.edu)